



1 **Title:**

2 Detection of agricultural flash droughts using impact-informed thresholds

3

4 **Ingrid Ubeda-Trujillo**^{1, 2, 3}, Micha Werner¹, Claudia Bertini¹, Miriam Coenders-Gerrits², and
5 Graham Jewitt^{1, 2}

6 ¹IHE Delft Institute for Water Education, P.O. Box 3015, 2601 DA Delft, the Netherlands

7 ²Delft University of Technology, Department Water Management. Section, P.O. Box 5048, 2600
8 GA Delft, the Netherlands

9 ³Universidad Nacional Autónoma de Nicaragua, UNAN-Managua. Rigoberto López Pérez
10 roundabout, 150m east.

11 Correspondence to: i.ubedatrujillo@tudelft.nl

12 **Abstract**

13

14 A rapid and sustained evaporative stress causes soils to lose moisture within days to weeks during
15 sensitive crop phases. This rapid soil depletion can severely affect agricultural systems and
16 manifest as events commonly referred to as agricultural flash droughts (AFDs). AFDs are often
17 detected using literature-based thresholds that assume uniformity across time and space. This
18 may, however, poorly represent the occurrence and impacts of AFDs in local contexts and limit
19 usefulness to decision-makers who require context-specific information. This study aims to
20 overcome these limitations by introducing an impact-informed calibration of the Standardized
21 Evaporative Stress Ratio (SESR) by linking SESR thresholds to observed crop losses.
22 Thresholds are derived temporally across crop management periods and spatially across soil
23 textures. The proposed calibration approach is tested in Nicaragua's Dry Corridor of Central
24 America, where rainfed agriculture predominates. Results suggest that although SESR exhibits
25 coherent evaporative stress signals during years with drought-induced crop losses, literature-
26 based thresholds showed limited skill in translating these signals into agriculturally relevant flash
27 drought detection across different crop management periods and soil textures. Threshold
28 performance varies across crop management periods and soil textures. Reliable thresholds could
29 not be detected in sandy soils, whereas clay-rich soils exhibited stable and skilful thresholds. In
30 loamy-silty soils, skilful thresholds were mainly observed during March and the pre-sowing
31 period, with limited skill thereafter. Validation results also showed that calibrated thresholds,
32 within the crop periods-soil combinations identified as skilful, successfully detected flash
33 drought events associated with crop losses more frequently than those reported in the literature.
34 Together, these findings indicate that monitoring AFD using impact-informed thresholds has an
35 operational value for drought management and can support better decision-making.

36

37 **Keywords:** Evaporative stress; Impact-informed thresholds; Crop management periods; Soil
38 Textures, Dry Corridor; Drought monitoring

39 **1. Introduction**

40

41 Drought is one of the major climate-related hazards affecting crop yields, particularly in
42 dryland regions dominated by rainfed systems (Kibler et al., 2023; Verbist et al., 2018). This
43 hazard thus undermines progress towards Sustainable Development Goals 1, 6 and 13.
44 Drought arises when a prolonged lack of precipitation leads to low water availability in the
45 soil, rivers, and reservoirs (Svoboda et al., 2002; Yuan et al., 2019). When these conditions
46 are further intensified by high temperatures and evaporative stress that increase rapidly and
47 persist over days to weeks, flash drought can develop (Basara et al., 2019; Noguera et al.,
48 2022). Under these conditions, soils lose water faster than it is replenished, causing abrupt



49 soil moisture decline and severely affecting agricultural systems (Yuan et al., 2019). When
50 such rapid depletion affects the sensitive crop growth stages in rainfed systems (Verbist et
51 al., 2018), the resulting conditions are commonly referred to as agricultural flash droughts
52 (AFDs) (Lovino et al., 2024). These events often evolve over only a few weeks, leaving
53 limited time for farmers and institutions to adjust planting decisions, resource allocation, or
54 short-term water management (Yuan et al., 2023). Because of the rapid onset and severe
55 impacts on rainfed agriculture, AFDs are a critical climate-related risk that needs to be
56 explicitly considered in early warning systems, risk management, and drought monitoring in
57 dryland regions.

58

59 A widely used approach for flash drought detection relies on the Standardized Evaporative Stress
60 Ratio (SESR), derived from the ratio of actual and potential evaporation (Edris et al., 2023; Otkin
61 et al., 2022). In most applications, flash droughts are detected based on SESR and literature-
62 based fixed percentile thresholds, implicitly assuming that a given percentile represents a
63 comparable level of stress across regions and seasons. Yet percentiles are purely relative
64 measures of rarity rather than of absolute stress, so a fixed percentile does not necessarily imply
65 the same level of plant and soil-water stress everywhere (Hobbins and Huntington, 2016; Otkin
66 et al., 2022). This assumption fails particularly in drylands with rainfed systems, because high
67 evaporative demand and chronically low soil moisture make evaporative stress part of the normal
68 background (Hobbins and Huntington, 2016; Kibler et al., 2023). In such settings, a fixed SESR
69 percentile threshold does not consistently distinguish anomalous evaporative stress from
70 background conditions across soil textures, and may not correspond to the same SESR levels at
71 which agricultural impacts occur (Suliman et al., 2024; Yu et al., 2023). These issues highlight
72 a broader methodological limitation of current SESR-based flash drought detection frameworks
73 when applied across diverse climate and soil conditions.

74 Moreover, thresholds used in the literature are usually defined independently of the crop
75 calendar, even though short dry spells during sensitive growth stages can cause damage (Verbist
76 et al., 2018), while a similar stress outside these windows has limited impact (Bucheli et al.,
77 2021; Teleubay et al., 2025). This creates a gap between when SESR anomalies are detected and
78 when impacts occur in the local context. Others indicator such as the Vegetation Health Index
79 (VHI) provides more direct evidence of agricultural stress on the ground, but it is reactive,
80 signalling stress only after it has occurred (Li et al., 2023; Rojas, 2020). In contrast, SESR
81 responds earlier to anomalies in the surface energy and water balance (Anderson et al., 2016;
82 Hobbins and Huntington, 2016), offering a timely physically based signal of evaporative stress
83 that has the potential to support operational use (Buitink et al., 2021; Leason et al., 2020; Li et
84 al., 2023; Teleubay et al., 2025) when appropriately calibrated (McEwen et al., 2021; Shyrokaya
85 et al., 2024). This suggests that SESR could support improved detection and monitoring of
86 agricultural relevant flash drought conditions if thresholds were calibrated to local agricultural
87 conditions and impact evidence. However, there is still no widely applied approach to
88 systematically calibrating SESR thresholds across both crop management periods and soil
89 textures, particularly in dryland, rainfed systems, which limits the operational relevance of SESR
90 for agricultural flash drought monitoring and management.

91 In many dryland regions, these limitations are particularly critical for smallholder rainfed
92 systems, where flash droughts can quickly translate into crop failure, food insecurity, and income
93 loss (Solh and van Ginkel, 2014) as has occurred in the Central American Dry Corridor of
94 Nicaragua, where recurrent drought episodes have been associated with declining crop yields
95 and heightened vulnerability among smallholder farmers. Strengthening agricultural flash



96 drought detection requires context-specific information that is essential for drought monitoring
97 and management. This study addresses these limitations by calibrating SESR thresholds
98 temporally across crop management periods and spatially across soil textures, using a benchmark
99 of agricultural impacts. To do so, this physically based but standardised indicator was linked to
100 locally observed drought-induced crop losses. The proposed approach aims to enhance the
101 agricultural relevance of SESR-based flash drought detection for farmers and decision-makers
102 in dryland, rainfed systems. Three main objectives were addressed: (i) to evaluate the potential
103 agricultural relevance of the Standardized Evaporative Stress Ratio (SESR) for detecting
104 anomalous evaporative stress during years with drought-induced crop losses, (ii) to calibrate and
105 evaluate SESR thresholds across crop management periods and soil textures, and (iii) to validate
106 literature-based and calibrated thresholds against locally independent agricultural benchmarks.
107 In a wider context, the impact-based calibration approach which was tested in the Dry Corridor
108 of Nicaragua offers a basis that could be adapted and tested in other dryland and rainfed regions
109 and can support the integration of local informed and impact-based agricultural flash drought
110 monitoring into drought management.

111 **2. Data and methods**

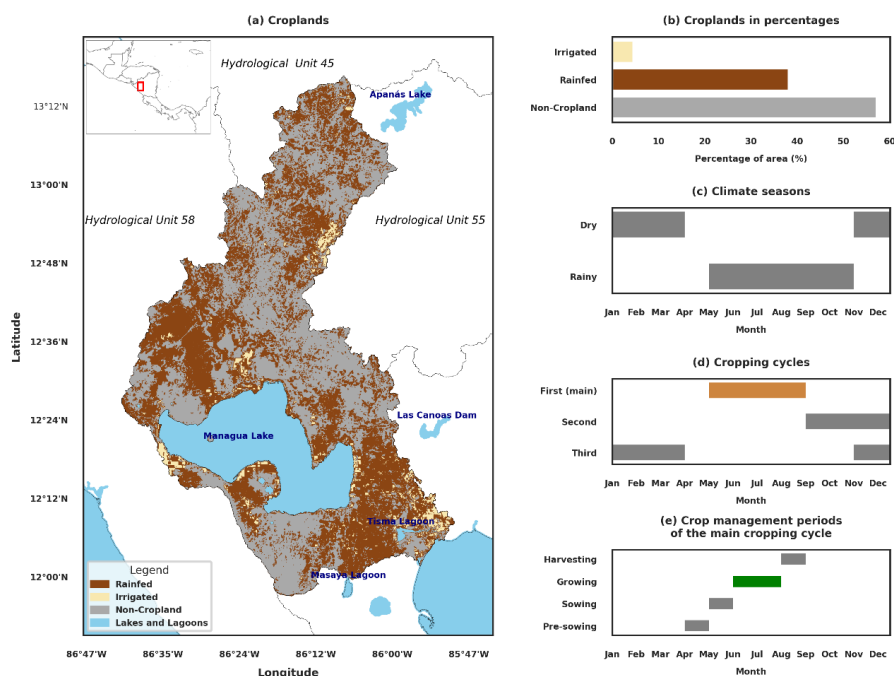
112 **2.1 Overview of the study area: climate, agricultural, and edaphic context**

113
114 To develop and test the calibration process, this study focuses on the Nicaragua Dry Corridor,
115 specifically in the northern portion of the Rio San Juan basin. This basin comprises eight
116 hydrological catchments and includes major rivers such as the Sinecapa and Pacora (INETER et
117 al., 2014). The basin spans diverse landscapes: The northern part overlaps with protected areas
118 including Yalí, Miraflor-Moropotente and Tizey-Estanzuela. The middle part includes Lake
119 Managua, several crater lagoons and additional protected areas, while the southernmost part
120 comprises the Tisma wetland, a Ramsar site. In total, the basin encompasses 31 municipalities
121 and approximately 640 settlements. At a broader scale, the study area forms part of the Central
122 America Dry Corridor, which includes the countries of Guatemala, El Salvador, Honduras, and
123 Costa Rica, bounded by the Caribbean region to the east and the Pacific Ocean to the west.

124
125 Figure 1a-b shows that rainfed agriculture covers approximately 40% of the study area
126 (Teluguntla et al., 2023; Ubeda Trujillo and Rocha, 2020) with subsistence and commercial
127 farming based on the main staples: beans and maize (van der Zee Arias et al., 2012). The main
128 cropping cycle extends from May to August (Figure 1d), lasting about four months and including
129 pre-sowing, sowing, growing (vegetative and flowering stages), and harvesting periods (Figure
130 1e). This cropping cycle coincides with the rainy season (Figure 1c). The average annual
131 precipitation is about 800 mm/year, and mean temperatures are above 25°C for the whole year
132 (van der Zee Arias et al., 2012). A notable climatological feature is the Canícula, a 10–20-day
133 mid-summer dry spell, commonly occurring from mid-July to August linked to the El Niño–
134 Southern Oscillation (Rojas et al., 2020). The Canícula temporally interrupts the rainy season
135 and tends to intensify during El Niño years (Verbist et al., 2018). Atmospheric evaporative
136 demand varies across climatic seasons and regions within the study area. Based on MOD16A2,
137 during the dry season, in the east-central and south-central parts of the Pacific plains (46–80
138 m.a.s.l.), potential evaporation (PET) reaches 8.5–9.3 mm day⁻¹ when aggregated over 10-day
139 periods. In contrast, in the north-eastern and western parts of the mountainous areas (682–1004
140 m.a.s.l.), PET ranges from 7.5–8.3 mm day⁻¹ (Salinas Marcenaro et al., 2023), reflecting elevated
141 atmospheric evaporative demand before the onset of rains. PET decreases in both regions during
142 the rainy season, with values of 4.5–6.0 mm day⁻¹ in the Pacific plains and 3.5–4.5 mm day⁻¹ in
143 the mountainous ranges (Salinas Marcenaro et al., 2023). Overall, the Pacific shows the highest



144 evaporative demand through the year, while the northern mountain region exhibits the lowest
 145 PET, following a common annual pattern governed by the transition from the rainy to the dry
 146 season. The study area is characterised by six soil textures (DGOT, 2024): (1) coarser sandy, (2)
 147 moderately coarse sandy, (3) loamy and silty, (4) moderately fine clay-loam, (5) fine clayey, and
 148 (6) very fine expansive clayey soils (see Figure S1).



149 Figure 1. Overview of the northern part of the Rio San Juan basin. (a) croplands, (b) cropland in
 150 percentage, (c) climate seasons, (d) cropping cycles, and (e) crop management periods of the
 151 main cycle.
 152

153 2.2 Data and preprocessing

154

155 Three main sources of data were used in this study: (1) MODIS MYD16A3GF (Steve et al.,
 156 2021), (2) Vegetation Health Index (FAO, 2014), and (3) qualitative information such as
 157 newspapers and reports. Qualitative information was compiled from the two oldest national
 158 newspapers in Nicaragua and from reports produced by GIEWS (Global Information and Early
 159 Warning System on Food and Agriculture; [https://www.fao.org/giews/reports/giews-](https://www.fao.org/giews/reports/giews-updates/en/)
 160 [updates/en/](https://www.fao.org/giews/reports/giews-updates/en/)), FEWS NET (Famine Early Warning Systems Network; <https://few.net/>), and EM-
 161 DAT (The International Disaster Database; <https://www.emdat.be/>).

162

163 The MODIS dataset provides 8-day composites at 500 m spatial resolution from 2001 to 2024.
 164 From this dataset, actual evaporation (ET) and potential evaporation (PET) inputs were used to
 165 derive the Standardized Evaporative Stress Ratio (SESR) and the standardized changes in SESR
 166 following the approach of Christian et al. (2019). Preprocessing included (i) computing the
 167 Evaporative Stress Ratio as ET/PET; (ii) calculating long-term mean and standard deviation at
 168 each time step and grid point; and (iii) standardizing ESR into Standardized Evaporative Stress
 169 Ratio (SESR) using a z-score transformation:



170
$$SESR_{ijp} = (ESR_{ijp} - \overline{ESR}_{ijp}) / \sigma ESR_{ijp} \quad (1)$$

171 Where $SESR_{ijp}$ is the z-score of ESR at specific grid point (ij) and time step p . ESR_{ijp} is the
 172 evaporative stress ratio; and σESR_{ijp} is the corresponding standard deviation across all years.
 173 (iv) computing temporal changes in SESR ($\Delta SESR$ -z):

174
$$(\Delta SESR_{ijp})_z = (\Delta SESR_{ijp} - \overline{\Delta SESR}_{ijp}) / \sigma \Delta SESR_{ijp} \quad (2)$$

176 Where $\Delta SESR_{ijp}$ is the change of SESR at specific grid point (ij) and time step p . $\overline{\Delta SESR}_{ijp}$ and
 177 $\sigma \Delta SESR_{ijp}$ are long-term mean and standardized deviation, respectively.

178
 179 The Vegetation Health Index (VHI) dataset has a 1 km spatial resolution and is available from
 180 1984 to 2024. Seven preprocessing steps are applied to ensure quality and temporal/spatial
 181 compatibility with SESR. This includes: (i) a range filtering that removes values outside the valid
 182 domain 0-1 (Kogan, 1995), (ii) an empirical saturation adjustment that smooths persistent
 183 maximum values (VHI =1) to reduce saturation artifacts (Gu et al., 2013), (iii) a conversion of
 184 decadal labels to ISO 8601 dates to ensure standardized time representation for further
 185 alignment; (iv) a resampling to 8-day intervals that aligns VHI to the temporal resolution of
 186 MODIS-based SESR products, (v) a linear temporal interpolation to 8-day resolution to fill
 187 temporal gaps and enable regular time-series analysis (Soltani et al., 2004), (vi) a spatial filling
 188 of voids through nearest-neighbour interpolation within valid data areas (Teoh et al., 2008), and
 189 (vii) a comparison of the original data with the final 8-day resampled version at various spatial
 190 points to evaluate the reliability of the harmonization process from the temporally interpolated
 191 dataset.

192 **2.3 Spatial and temporal calibration approach**

193 The spatial and temporal calibration of SESR approach proposed here is summarized in six parts.
 194 The spatial and temporal sampling design is presented in Sect. 2.3.1. The baseline benchmarks
 195 of drought-induced crop losses are described in Sect. 2.3.2. The detection of agricultural flash
 196 droughts is detailed in Section 2.3.3. In Sect. 2.3.4, a diagnostic assessment of the Standardized
 197 Evaporative Stress Ratio (SESR) is conducted prior to calibration. The calibration of SESR
 198 thresholds, including performance metrics and uncertainty analysis, is introduced in Sect. 2.3.5.
 199 Finally, the validation strategy for literature-based and calibrated SESR thresholds is presented
 200 in Sect 2.3.6.

201 **2.3.1 Spatial and temporal sampling design**

202 The period of analysis was from February to August from 2000-2024. February to April is
 203 considered an early warning opportunity period, since early evaporative stress signals during
 204 these months may condition soil moisture availability before the sowing period. April is a critical
 205 pre-sowing month, as high evaporative stress during this month can reduce germination success
 206 ahead of sowing. Farmers typically prepare the land and make sowing decisions (Verbist et al.,
 207 2018). Sowing typically occurs in May, with the main growing stages of maize and beans in
 208 June-July, while August is the end of the main cropping cycle. To represent the spatial dimension
 209 sample locations are distributed across six soil texture classes in rainfed areas (see Figure S1),
 210 allocated proportionally to ensure a representative sample in each soil texture class, resulting in
 211 a sampling interval of about 3 km and 388 time series of 8-day SESR values.

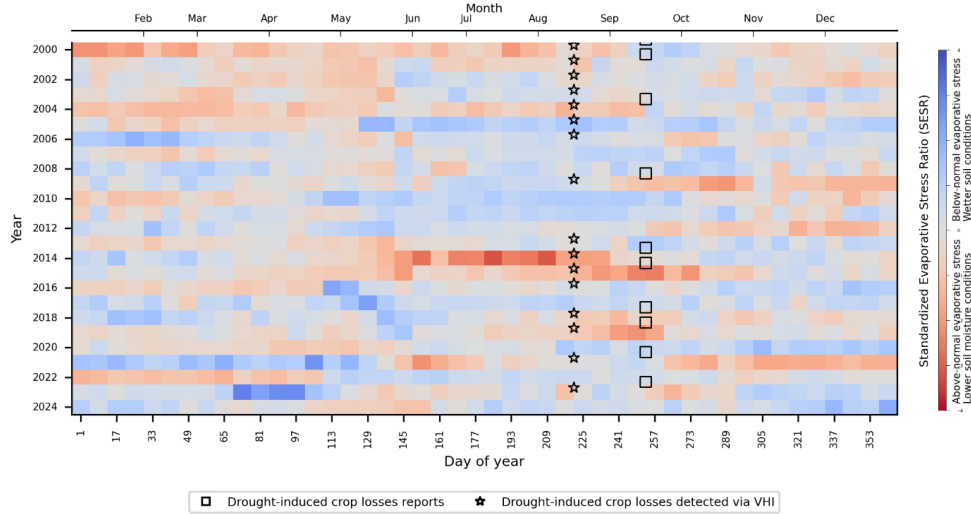
212



213 2.3.2 Impact benchmarks of drought-induced crop losses

214 Two agricultural-impact benchmarks related to drought-induced crop losses were created: one
215 based on Vegetation Health Index (VHI) and a second derived from newspapers and reports
216 (Figure 2). The VHI-based benchmark was used to identify impact-relevant years for calibration,
217 whereas both benchmarks were used to validate literature-based and calibrated SESR thresholds.
218 The benchmarks were obtained as follows:

- 219 (i) Years with drought-induced crop losses were obtained from the Vegetation Health
220 Index (FAO, 2014). Crop losses were detected when VHI values at the end (in
221 August) of the first cropping cycle fell below 0.35 (Fuganti et al., 2020). This
222 criterion was applied independently at each sample location, each represented by
223 independent time series. The resulting time series were then grouped by soil texture
224 classes. Note that Figure 2 indicates the occurrence of crop loss impacts at one
225 sample location and does not necessarily imply region-wide impacts.
- 226 (ii) Years with drought-induced crop loss reports were obtained from the two main
227 national newspapers, as well as from the GIEWS, FEWS NET, and EM-DAT
228 databases. Digital archives were systematically searched using drought- and impact-
229 related keywords in Spanish and English, including "drought", "sequía", "lack of
230 rain", "falta de lluvia", "lluvias tardan en llegar", "crop loss (es)", "pérdida de
231 cosecha", "yield reduction", and combinations of these terms. For each candidate
232 newspaper article or report, the information was organized into three levels of detail,
233 each presented separately. The first level includes the date and a short description of
234 the reported impacts for each source. The second level provides the dates, the type of
235 impacts reported (e.g. economic, agricultural, population affected), and the sources.
236 The third level summarizes the year, the crop impacts, and the sources reporting those
237 impacts. Documented drought-induced crop loss events were retained only when
238 reported by at least three independent sources. With respect to timing, newspapers
239 usually report drought-related impacts from July onwards in the same year as the
240 drought event occurs, which is the middle of the main cropping cycle under study.
241 However, some international reports are reported in the year after the drought event.
242 To harmonise the timing of reported impacts, each reported event was constrained to
243 a one-month window centred on September. Crop losses reported between January
244 and April were interpreted as impacts of drought events that occurred in the previous
245 year. From a spatial perspective, crop loss impacts were inconsistently documented
246 and spatially heterogeneous across municipalities and, consequently, across soil
247 texture classes within the study area. Therefore, the drought-induced crop loss was
248 interpreted as representative of broader regional conditions rather than as spatially
249 explicit observations at the soil texture scale.



250

251 Figure 2 Years with crop losses derived from the Vegetation Health Index and reports at one
 252 representative sample location within the study area characterise by moderately fine clay-loam
 253 soil. The heatmap represents the median of the Standardized Evaporative Stress Ratio (SESR)
 254 across the sampled locations and aggregated at each 8-day interval.

255

256 2.3.3 Detection of agricultural flash droughts

257 In the Standardized Evaporative Stress Ratio (SESR) framework described by Christian et al.,
 258 (2019), a flash drought event is identified using percentile thresholds applied to SESR and the
 259 rate of change of SESR (Δ SESR), together with a minimum duration requirement. Drought is
 260 classified when SESR falls below the 20th percentile of the distribution of SESR values, and the
 261 event becomes a flash drought when rapid and sustained intensification of evaporative stress
 262 persists for about 30 days. The rapid intensification is detected when Δ SESR crosses the 40th
 263 percentile of the distribution of Δ SESR values and when the average Δ SESR during the entire
 264 event remains below the 25th percentile. These thresholds have been equally applied in other
 265 studies (cf. Gou et al., 2022; Nguyen and Choi, 2024). This study refines this framework by
 266 replacing the fixed 20th percentile threshold with a calibrated threshold specific to crop
 267 management periods and soil texture.

268

269 When drought conditions are sustained, they signal an increase in evaporative stress, which in
 270 turn raises the likelihood of soil moisture decline and associated agricultural impacts. Based on
 271 this rationale, agricultural flash droughts (AFDs) in this study were detected when SESR dropped
 272 below a defined threshold ($\theta_{t,s}^*$), accompanied by an intense and sustained evaporative stress
 273 confirmed using the 40th and 25th percentile thresholds of the Δ SESR (Christian et al., 2019).
 274 Accordingly, an AFD was defined as:

275

$$276 \text{AFD}_{t,k} = \begin{cases} 1, & \text{if } \text{SESR}_{t,s} \leq \theta_{t,k} \wedge \Delta \text{SESR}_{t,k} \leq P_{40} \text{ (1 exception allowed)} \wedge \overline{\Delta \text{SESR}}_{\text{AFD},p} \leq P_{25} \\ 0, & \text{Otherwise} \end{cases} \quad (3)$$

277 Where $\text{AFD}_{t,k}$ denotes the presence (1) or absence (0) of an agricultural flash drought. $\text{SESR}_{t,k}$
 278 is the Standardized Evaporative Stress Ratio across crop management period t and sample k
 279 falling in soil texture. $\theta_{t,k}$ is the SESR threshold to be calibrated. $\Delta \text{SESR}_{t,k}$ is the change of
 280 SESR between consecutive time intervals. P_{40} is the 40th percentile of Δ SESR values. P_{25} is the

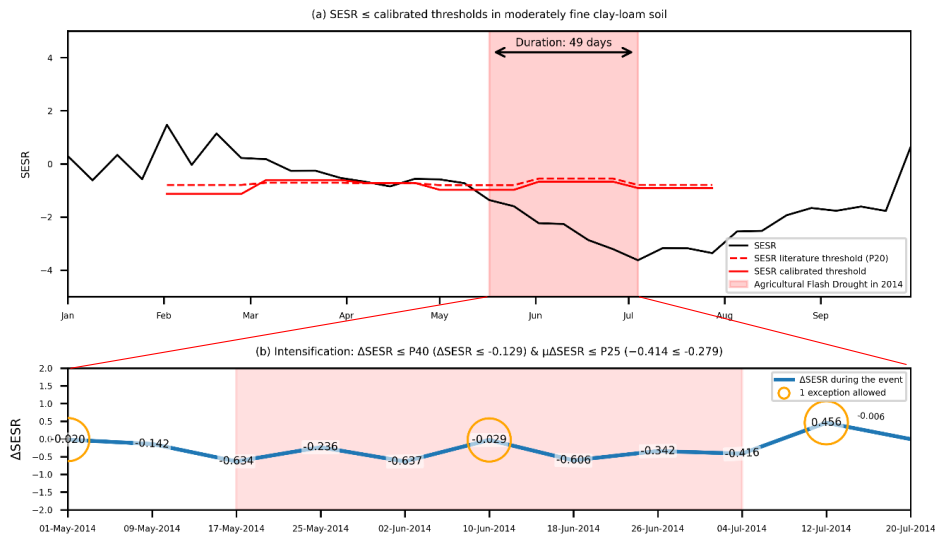


281 25th percentile threshold of ΔSESR . $\overline{\Delta\text{SESR}}_{AFD,p}$ is the mean ΔSESR over the full agricultural
 282 flash drought period. \wedge denotes the logical "and" condition.

283

284 Figure 3 illustrates an agricultural flash drought (AFD) event in 2014 in fine clay-loam soil at
 285 one of the sample points. Panel (a) shows the SESR trajectory (black line) together with the
 286 calibrated threshold (red dashed line). From mid-May to early July, SESR dropped below the
 287 calibrated thresholds for 49 consecutive days. Panel (b) provides the ΔSESR during the event.
 288 Rapid intensification is confirmed when consecutive ΔSESR values remained below the 40th
 289 percentile, with only one exception allowed, which is marked here with an orange circle. The
 290 mean (μ) of the ΔSESR across the event also remained below the 25th percentile, reinforcing its
 291 classification as an AFD. In the figure, the actual $\mu(\Delta\text{SESR})$ and the 40th and 25th percentiles of
 292 the time series are shown to better illustrate the example. Detection therefore requires both
 293 sustained low SESR and rapid intensification, with the calibrated SESR threshold governing the
 294 event onset in this example.

295



296

297 Figure 3 Time-series schematic showing how calibrated SESR thresholds and rapid
 298 intensification of SESR are used to detect agricultural flash drought in 2014. (a) SESR evolution
 299 relative to the literature-based threshold (P20) and the calibrated threshold ($\theta_{t,k}$). The shaded
 300 period indicates the detected agricultural flash drought, which begins when SESR first falls
 301 below the calibrated threshold (On May 17) and persists until recovery due to the criteria for
 302 ΔSESR being above the representative threshold. (b) Corresponding changes of SESR (ΔSESR)
 303 during the same period, used to confirm rapid intensification.

304 2.3.4 Diagnostic assessment of the agricultural relevance of SESR prior to calibration

305 Three diagnostic assessments were conducted to assess whether SESR functions as a potential
 306 agricultural indicator of evaporative stress linked to drought-induced crop losses. The first
 307 assessment examines the consistency between SESR and Vegetation Health Index (VHI) using
 308 aggregated data from all soil textures across the sample locations. To achieve this, a linear
 309 regression and Pearson correlation analyses were performed between SESR and VHI using two
 310 representative years: one with confirmed crop losses caused by drought and one with no reported
 311 losses.



312 The second assessment analyses the distribution of evaporative stress across crop management
313 periods and soil texture classes. Its aim is to determine whether evaporative stress (SESR) differs
314 between years with drought-induced crop losses and non-drought years when no losses occurred,
315 with the VHI benchmark used to identify years with drought-induced crop losses. For each
316 sample location the SESR time series were extracted in their original 8-day resolution for the
317 period from February to July. Two datasets of SESR values were then created, one for years with
318 and one for years without drought-induced crop losses. The distribution of the SESR values were
319 visualised using boxplots by crop management periods and soil texture classes. As most SESR
320 distributions deviated from normality (tested using Shapiro–Wilk normality test) (Ghasemi and
321 Zahediasl, 2012), non-parametric tests, including Mann–Whitney U and Kolmogorov–Smirnov
322 tests (Sawilowsky, 2005) were applied. Significant differences ($p < 0.05$) indicated that the SESR
323 distributions differed between drought-induced crop loss and non-drought years.

325 2.3.5 Calibration of SESR thresholds, performance metrics, and uncertainty-based selection

326
327 The calibration aimed to identify SESR threshold values that best separate years with and without
328 drought-induced crop losses by maximising the F_β score, thereby determining the evaporative
329 stress associated with the occurrence of agricultural impacts. SESR threshold calibration was
330 performed from 2000 to 2013 using SESR datasets constructed in Section 2.3.4, stratified by
331 crop management periods and soil texture classes. Within each stratum, SESR observations were
332 classified into two classes, positive and negative, corresponding to years with and without
333 drought-induced crop losses. As the number of SESR time series (sample locations) were
334 imbalanced between classes, inverse-frequency weighting was applied (Cao et al., 2019).
335 Subsequently, these classes were used jointly during thresholds optimisation to evaluate
336 candidate SESR thresholds. A set of candidate thresholds was defined as SESR values ranging
337 between the second and ninety-fifth percentiles of the SESR distributions. For each candidate
338 threshold, SESR values were converted into a binary classification distinguishing drought-
339 impact conditions from non-impact conditions. These candidate thresholds were evaluated using
340 an empirical-utility maximisation approach (Nan et al., 2012), in which thresholds were selected
341 by maximising the F_β score ($\beta = 0.3$) for each crop management period and soil texture. For each
342 candidate threshold, precision and recall were first computed and then the corresponding F_β score
343 was derived. Precision represents the proportion of true positive results among all events
344 classified as positive, whereas recall represents the proportion of true positive detections among
345 all actual positive events in the data. The parameter β controls the relative weighting of precision
346 and recall through the β^2 terms, with lower values (≤ 0.5) of β placing greater emphasis on
347 precision and higher values (≥ 0.5) increasing the contribution of recall to the F_β score. The F_β
348 metric is expressed as:

$$349 \quad F_\beta = \frac{(1 + \beta^2) P \cdot R}{\beta^2 P + R} \quad (4)$$

350 where P is precision, R is recall, and the F_β score represents an adjusted balance that weights P
351 and R depending on the value of β . β is set to 0.3 to represent the preference of stakeholders for
352 missed events over false alarms (Guimarães Nobre et al., 2023). During calibration, the tested
353 candidate thresholds were explored using a 0.01 step size for fine exploration. A time step was
354 classified as drought when the SESR value fell below the candidate threshold. To assess
355 threshold robustness, the stability of the calibrated thresholds was evaluated by quantifying
356 sampling uncertainty using cluster-level bootstrapping (Padiyedath Gopalan et al., 2019) with
357 1000 replicates (Efron and Tibshirani, 1986). The bootstrap was applied at the year–location
358 level, resampling complete SESR time series (February–July) with replacement. Each bootstrap
359 replicate produced an optimal threshold, and the resulting empirical distribution of calibrated
360 thresholds was summarised using the median, standard deviation, and 95% confidence interval



361 (CI95%) to characterise variability and uncertainty. In addition to uncertainty assessment, the
 362 calibrated thresholds were also assessed using the false alarm rate (FAR) and Receiver Operating
 363 Characteristics Curve (ROC) and its Area Under Curve (AUC). Lower FAR values (≤ 0.2)
 364 indicate fewer false drought detections, whereas higher FAR values (≥ 0.5) indicate a higher
 365 frequency of false alarms. AUC values greater than 0.5 indicate that the thresholds provide
 366 discriminatory ability between years with and without drought-induced crop losses (Marzban,
 367 2004). These performance and uncertainty metrics, together with the precision metric, were used
 368 to select the final set of calibrated thresholds, retaining only those values of thresholds as skilful
 369 that simultaneously satisfy the following criteria: precision ≥ 0.70 , FAR ≤ 0.30 , ROC-AUC \geq
 370 0.60, and CI95% ≤ 0.40 . These criteria were chosen to approximate likely stakeholder
 371 preferences for reliable drought detection with limited false alarms, while maintaining acceptable
 372 discriminatory skill and stable thresholds estimates.

373

374 2.3.6 Validation strategy of literature-based and calibrated SESR thresholds

375 Using two validation metrics, the validation step assessed the ability of both literature-based and
 376 calibrated SESR thresholds to identify flash drought events for each crop management period
 377 and soil texture that coincide with years associated with drought-induced crop losses. The
 378 validation was performed only for the skilful thresholds identified during calibration, as
 379 described above. SESR thresholds validation was conducted from 2014 to 2024 using two
 380 distinct agricultural benchmarks: (1) drought-induced crop loss signals derived from the VHI
 381 and (2) documented historical drought-induced crop losses reported. The first validation metric
 382 (V_1) was defined as:

$$383 \quad V_1 = \begin{cases} 1, & FD_t = 1 \text{ and } cl_t = 1 \\ 0, & \text{otherwise} \end{cases} \quad (5)$$

384 Where V_1 represents the validation criterion, FD_t denotes a flash drought event identified at time
 385 t , and cl_t represents the crop loss condition at the end of the first cropping cycle (here, August).
 386 A second validation metric (V_2) was defined to assess whether flash drought events coincide with
 387 reported drought-induced crop losses:

$$388 \quad V_2 = \begin{cases} 1, & \text{if } FD_t = 1 \text{ and } dci_t = 1 \\ 0, & \text{otherwise} \end{cases} \quad (6)$$

389

390 Where V_2 represents validation criterion, and dci_t denotes documented drought-induced crop
 391 impacts for September, as defined in developing the impact benchmark.

392 3. Results

393 3.1 Agricultural relevance of the Standardized Evaporative Stress Ratio (SESR)

394 Figure 4 presents the regression equations and correlation coefficient that describe the
 395 relationship between SESR and VHI in both conditions for a year (2014) with and without (2013)
 396 drought-induced crop losses. Although the relationship between SESR and VHI is positive in
 397 both years, a smaller slope ($b=1.49$) and correlation ($r=0.29$) in 2013 indicate a weak
 398 relationship, while in 2014 the clearer slope ($b=3.94$) and correlation ($r=0.63$) suggest a stronger
 399 vegetation response to evaporative stress during drought years with confirmed crop losses. The
 400 distribution of SESR values at the lower VHI values indicates poor vegetation health and aligns
 401 with more negative SESR values, reflecting stronger evaporative stress. Although correlation
 402 does not imply causation, the fact that these differences emerge even in a naturally dry
 403 environment like the Dry Corridor indicates that SESR provides a meaningful signal that is
 404 coherent with vegetation stress during drought years with confirmed crop losses.

405

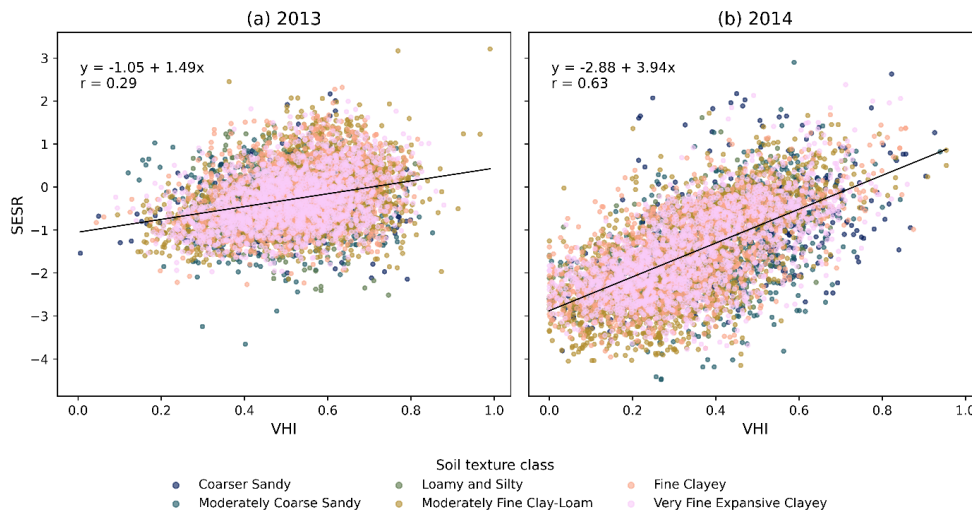


406 Boxplots of SESR distributions (Figure 5), together with the statistical difference tests (see
407 Figure S2), illustrate how evaporative stress varies across crop management periods and soil
408 textures between years with and without drought-induced crop losses. During February and
409 March, SESR distributions exhibit strong overlap in both medians and interquartile ranges
410 (IQRs), indicating limited separation between conditions. From April onwards, separation begins
411 to emerge, with the clearest differences occurring in May–July, when years with drought-
412 induced crop losses consistently show lower SESR medians across all soil textures. This
413 separation is weakest in coarse sandy soils, where IQRs remain large and strongly overlapping.
414 In contrast, it is strongest in finer-textured soils (moderately fine clay loam, fine clayey, and very
415 expansive clayey), where a persistent downward shift in the median occurs without a
416 corresponding increase in distributional spread. During June–July, separation further increases
417 due to more frequent and more negative SESR values, particularly in fine-texture soils,
418 indicating that the late period differences arise from both shifts in typical conditions (lower
419 medians) and enhanced lower tail behaviour.

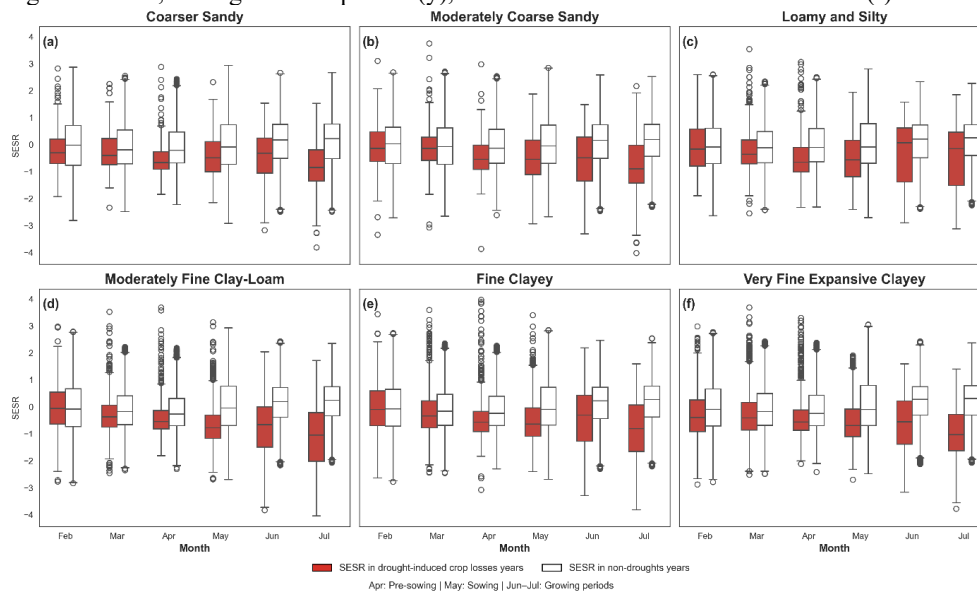
420

421 The relatively low discrimination of SESR in sandy soils between drought-induced crop loss
422 years may be explained by their high permeability and low water-holding capacity (Jabro et al.,
423 2009; Wankmüller et al., 2024), which cause rapid responses to evaporative demand even in
424 years without crop losses. Consistent with this behaviour, statistical tests show no significant
425 differences in SESR between years for sandy soils (Figure S2). In contrast, the stronger
426 discrimination observed in clay-rich soils is likely linked to their higher water retention capacity
427 (Or and Lehmann, 2019; Sun et al., 2019), which allows evaporative stress signals to persist
428 longer and enhances the contrast in SESR between drought-induced crop loss and no-drought
429 years. This separation is supported by statistically differences ($p < 0.05$) in both tests (Figure
430 S2). Moreover, the upper and lower tails of the SESR distribution in these soils exhibit
431 comparable lengths, indicating that the area experiences a balanced range of extreme transitions
432 rather than being dominated exclusively by drying or wetting anomalies. This balance enables
433 SESR to capture both the intensification and easing of evaporative stress, thereby supporting a
434 more reliable identification of stress related thresholds.

435



436
 437 Figure 4. Scatterplots of the relationship between SESR and VHI from February to July in (a)
 438 2013 (year without drought) and (b) 2014 (drought year with confirmed crop losses), with data
 439 aggregating across all soil textures at the sample locations. Each panel includes the fitted linear
 440 regression line, the regression equation (y), and the Pearson correlation coefficient (r).



441
 442 Figure 5 Panel (a)–(f) Standardized Evaporative Stress Ratio (SESR) aggregated across crop
 443 management periods and soil texture classes at the sample locations for years with and without
 444 drought-induced crop losses.

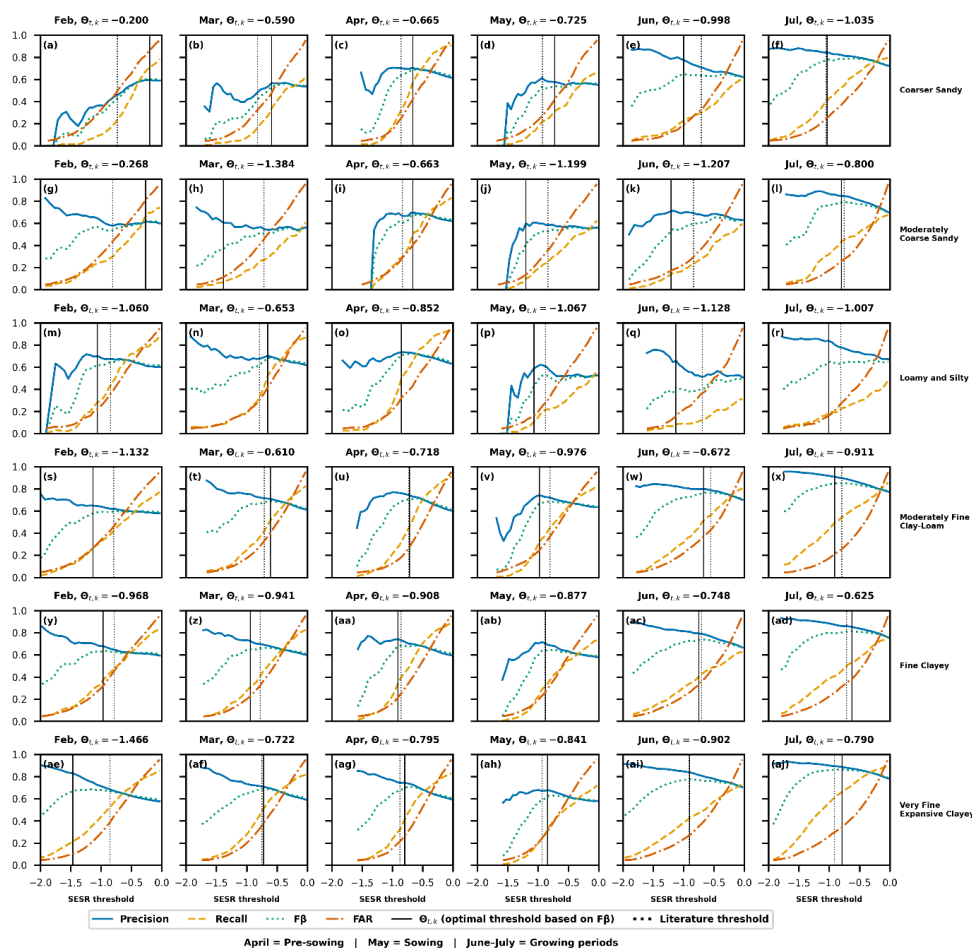
445 **3.2 Performance of calibrated SESR thresholds across crop management period and soil**
 446 **textures**

447 Figure 6 shows how the median performance metrics of precision, recall, FAR (False Alarm
 448 Rate) and F_β vary as the value of the thresholds $\theta_{t,k}$ (Eq. 3). This allows identification of the



449 thresholds for each crop management period and soil texture that achieves the best combination
450 as expressed by F_{β} . In each panel, the calibrated threshold ($\theta_{t,k}$) is indicated by a solid vertical
451 line, with the value indicated in the title. The literature-based threshold is shown as a dotted
452 vertical line reference. While Figure 6 illustrates the overall median behaviour of the metrics
453 across the thresholds range, the numerical values discussed below refer specifically to the values
454 of the performance metrics at the calibrated thresholds. Figure 7 summarizes where SESR
455 thresholds exhibit skill across periods and soils.

456 In all soil textures, higher values of the SESR thresholds increases recall and FAR and decreases
457 precision. The metric combinations at the F_{β} maximum differ across soil textures and crop
458 management periods. During the pre-sowing period (April), loamy and silty soils exhibit
459 calibrated thresholds with balanced precision (≈ 0.83) and recall (≈ 0.68), while coarser sandy
460 soils show lower recall (≈ 0.43 – 0.66) and higher FAR (> 0.20). During the sowing period (May),
461 most soils are characterised by calibrated thresholds with reduced recall (< 0.45) and FAR
462 typically below 0.12, including moderately coarse sandy, loamy–silty, and clay–loam soils. In
463 contrast, during the growing period (June–July), calibrated thresholds in nearly all soil textures
464 have high precision (> 0.84) and low FAR (< 0.12), while recall varies across soils, ranging from
465 approximately 0.32 in coarser sandy soils to above 0.68 in fine and very fine clayey soils. Lower
466 discrimination skills is mainly observed during the pre-sowing (April), and sowing (May) periods
467 for several soil textures, including coarse sandy, moderately coarse sandy, and loamy–silty soils
468 ($AUC \leq 0.70$, Figure 7). In contrast, higher discrimination skill is consistently observed during
469 the growing period (June–July) across most soil textures, with AUC values commonly
470 exceeding 0.80 and reaching above 0.90 in fine and very clayey soils for individual sample
471 points.



472

473

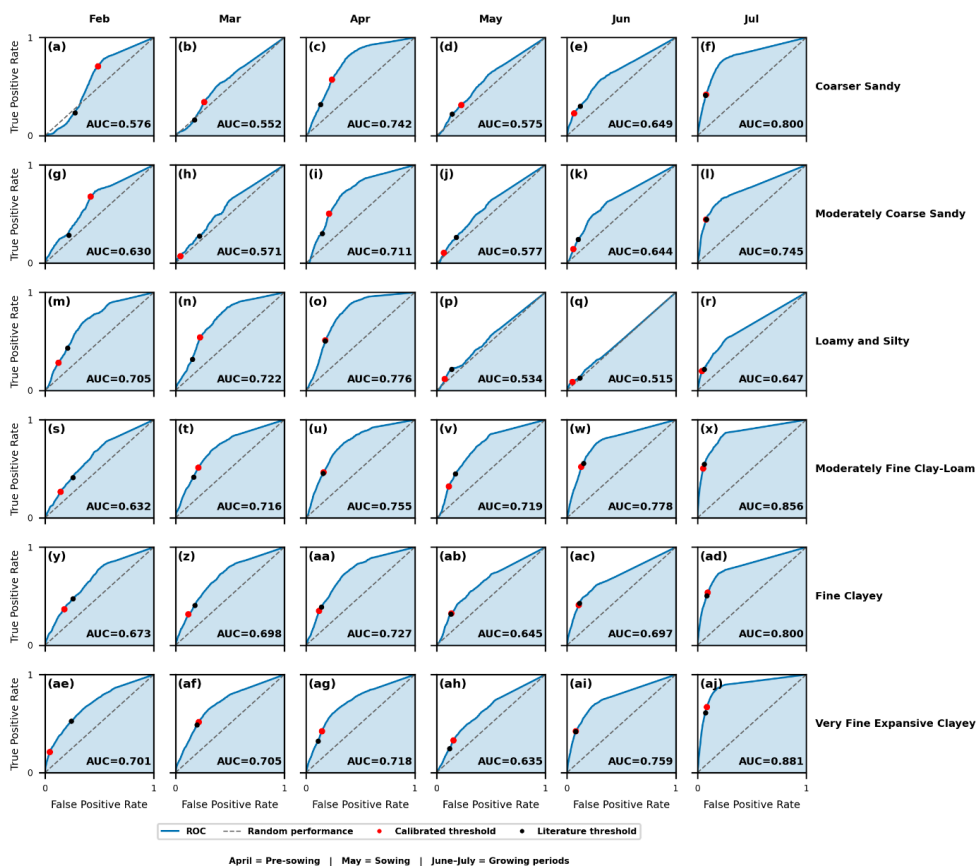
474

475

476

477

Figure 6 Median performance metrics of SESR thresholds across crop management periods and sample points for each soil texture, including precision, recall, $F\beta$, and False Alarm Rate (FAR) evaluated over the full thresholds range. Solid vertical line denotes the optimal calibrated thresholds ($\theta_{t,k}$), while the dotted vertical line shows reference thresholds from literature. Note that the z-score of the literature thresholds is derived from the empirical distribution of SESR.



478

479

480

Figure 7 Median Receiver-Operating Characteristics Curve (ROC) values across crop management periods and sample points for each soil textures.

481

3.3 Stability and uncertainty of SESR thresholds

482

483

484

485

486

487

Figure 8 show the uncertainty in the optimal SESR-based thresholds across crop management periods and soil textures, expressed by the CI95 metric. Cells with a solid black outline indicate soil-month combinations for which the thresholds simultaneously satisfy the predefined criteria: precision ≥ 0.70 , FAR ≤ 0.30 , ROC-AUC ≥ 0.60 , and CI95% ≤ 0.40 . Only these thresholds were retained for validation.

488

489

490

491

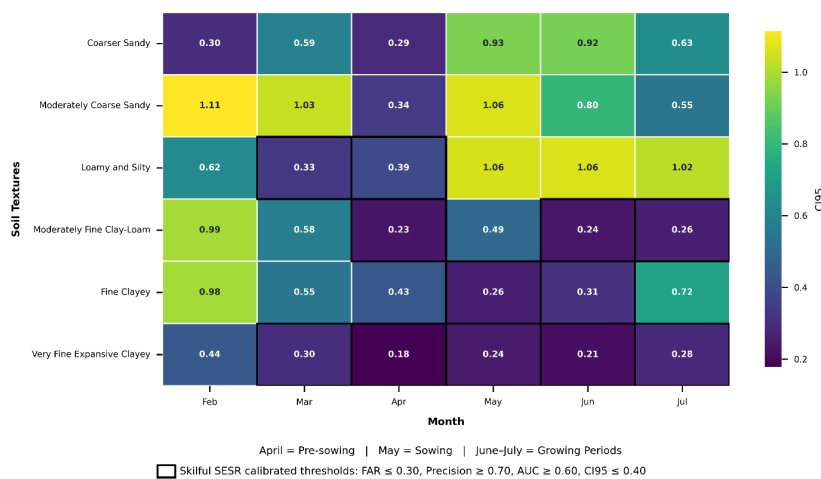
492

493

494

495

Threshold uncertainty varies across both crop management periods and soil textures. Sandy soils (coarse sandy and moderately coarse sandy) exhibit the highest CI95 range during the selected period. In contrast, intermediate and fine-textured soils show lower CI95 range. Skilful thresholds are identified for loamy and silty soils during March and April (pre-sowing period), for moderately fine clay-loam soils during April and June–July (growing period), and for very expansive clayey soils from March through July (growing period). Fine clayey soils show intermediate uncertainty, with CI95 ranges exceeding the selection threshold in most months. Figure S3 illustrates the full distribution of the calibrated SESR thresholds.



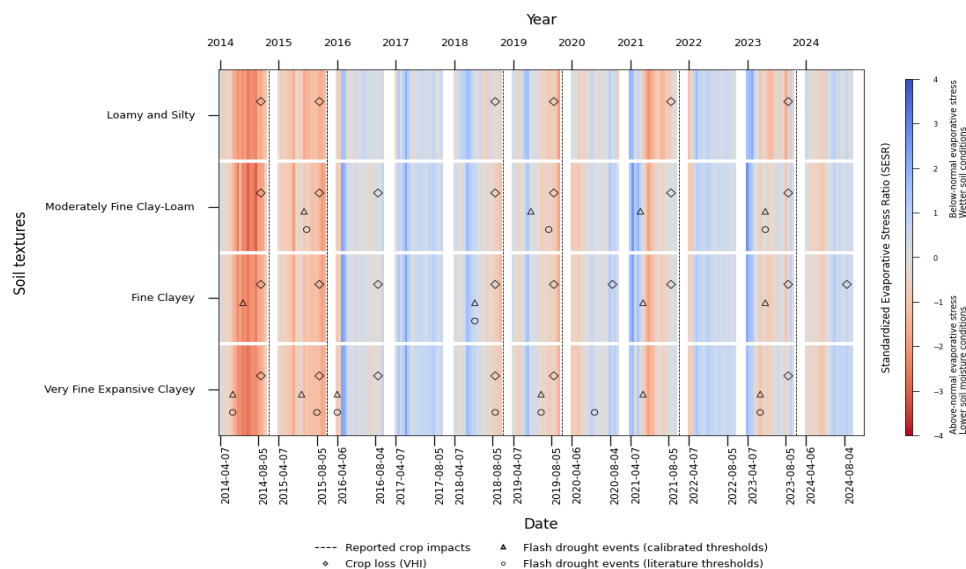
496

497 Figure 8 Uncertainty level of optimal thresholds by crop management periods and soil textures.
 498 The black cell shows the optimal thresholds that simultaneously satisfied the following criteria:
 499 precision ≥ 0.70, FAR ≤ 0.30, ROC-AUC ≥ 0.60, and CI95% ≤ 0.40.

500 3.4 Validation of literature-based and calibrated SESR thresholds

501

502 Figure 9 illustrates years in which flash droughts are detected using calibrated thresholds and
 503 literature-based thresholds for the validation period (2014-2024), and how these align against
 504 years with crop losses. This shows that flash drought events that are detected using calibrated
 505 thresholds appear in more years and across more soil textures than those detected using literature-
 506 based thresholds. In moderately fine clay-loam, fine clayey, and very fine expansive clayey soils,
 507 calibrated thresholds detections are present in several years in which crop losses are also shown.
 508 In contrast, detections based on literature thresholds are absent or limited to fewer years for these
 509 same soils. In loamy and silty soils, both calibrated and literature-based flash drought detections
 510 occur less frequently, and several years with crop losses do not show a corresponding flash
 511 drought detection. Across all soil textures, there are also years in which flash drought detection
 512 occur without accompanying crop losses, and years in which crop losses occur without flash
 513 drought detections. Supplementary Figures S4 and S5 summarise the hit rates between flash
 514 droughts detected using literature (column left) and calibrated-based thresholds versus crop
 515 losses detected via VHI and reports. For all soil textures, hit rates are zero or low during the pre-
 516 sowing and sowing periods. During the growing period (June-July), calibrated thresholds yield
 517 consistently higher hit rates than literature-based thresholds across all soil textures, with the
 518 highest values observed in moderately fine clay-loam and fine clayey soils. In contrast, hit rates
 519 associated with literature-based thresholds remain low across all periods and soil textures.
 520



521
522 Figure 9 Temporal alignment of flash droughts events and crop losses identified via VHI and
523 newspapers/reports. The 8-day SESR time series for each soil texture is shown as the background
524 over the evaluation period. Flash drought events detected using calibrated and literature-based
525 thresholds, together with reported crop losses, are overlaid.

526 **4. Discussion**

527 **4.1 Relevance of SESR in detecting agricultural flash droughts**

528

529 Results show that the Standardized Evaporative Stress Ratio (SESR) captures a coherent signal
530 of higher evaporative stress during years in which crop losses are observed, as indicated by
531 contrasts in the SESR-VHI relationship between non-drought and drought years (Figure 4). This
532 indicates that SESR is coherent with vegetation stress during years with confirmed crop losses,
533 and consistent with the mechanism whereby vegetation becomes increasingly sensitive to
534 evaporative stress once soil moisture constraints emerge, while under non-limiting conditions
535 changes in evaporative demand do not translate into physiological stress (Anderson et al., 2016;
536 Hobbins and Huntington, 2016; Kozłowski, 1968). However, translating this signal into an
537 indicator of agricultural flash drought depends on how the onset threshold is defined within the
538 detection approach (Section 2.3.3). Analysis of the distribution of SESR values (Figure 5) shows
539 that more extreme SESR values occur during years with drought-induced crop losses. Although
540 literature-based and calibrated thresholds are derived separately for each crop management
541 period and soil texture, they approach similar values in a limited number of cases (Figure 6), this
542 behaviour is not consistent across soil textures and crop management periods. This inconsistency
543 arises because literature-based thresholds are defined solely by the statistical properties of the
544 SESR distribution (Christian et al., 2019), whereas calibrated thresholds are constrained by the
545 occurrence of observed crop losses (see sections 2.3.2, 2.3.3, 2.3.5), leading to different SESR
546 values being identified as agriculturally relevant even within the same soils texture and
547 management period. In the dry corridor of Central America, drought-induced crop losses occur
548 at SESR levels that depend on this approach rather than on percentile exceedance alone (see



549 Figures S4, S5). Consequently, calibrating using agricultural impact information improves the
550 consistency in which SESR identifies agriculturally relevant flash droughts, compared to the use
551 of fixed percentile threshold alone (Section 2.3.5).

552 This limitation in how flash drought onset is defined also has direct operational consequences
553 for the alignment between detected events and observed crop losses. The default threshold
554 ignores agricultural context and cannot be directly linked to the occurrence of crop losses. When
555 detection occurs outside pre-sowing, sowing and growing periods, its operational value is limited
556 (Bucheli et al., 2021), meaning that the occurrence of flash drought may then not correspond to
557 crop losses (Teleubay et al., 2025), consistent with the low hit rates in Figures S4-S5. These
558 limitations are reflected in the less consistent temporal alignment between literature-based
559 detections and documented crop losses years, compared to the calibrated thresholds (Figure 9).
560 Together, the results demonstrate that SESR provides signals of evaporative stress relevant for
561 agricultural flash drought detection, but that in this dryland system such relevance requires
562 context-specific, impact informed calibration rather than fixed percentile thresholds (Halwatura
563 et al., 2017). These finding are also with a core principle of impact-based forecasting, namely
564 that hazard signals must be translated into locally relevant impact thresholds to support
565 meaningful early warning and decision-making (McEwen et al., 2021; Shyrokaya et al., 2024).

566 **4.2 Behaviour of calibrated SESR thresholds across soil textures and crop management** 567 **periods to detect agricultural flash droughts**

569 The response of calibrated SESR thresholds across soil textures and crop management periods
570 shows that flash drought detection depends on both the temporal evolution of evaporative stress
571 and the capacity of each soil texture to store and release moisture during crop management
572 periods. In the Dry Corridor in Nicaragua, high atmospheric demand marked by the transition
573 between the dry season and the rainy season produces rapid fluctuations in soil moisture (Son et
574 al., 2018). Because local maize and bean systems rely almost entirely on precipitation (van der
575 Zee Arias et al., 2012), these moisture fluctuations coincide with short-term stress conditions
576 that are reflected in SESR variability during drought years (Figure 5), thereby shaping the
577 variability of SESR signals used for onset detection.

579 Coarse and moderately sandy soils, with rapid drainage and low water capacity (Jabro et al.,
580 2009; Wankmüller et al., 2024), generate short-lived and highly variable evaporative stress. As
581 a result, SESR anomalies are less persistent and less clearly associated with crop losses, making
582 the distribution of SESR values (Figures 5a,b) difficult to discriminate between years with and
583 without identified crop losses (Figure 2), and resulting in calibrated thresholds characterised by
584 high uncertainty (Figure 8). In contrast, clay-rich soils, characterised by greater water retention
585 and slower drainage (Jabro et al., 2009), allow evaporative stress to persist over longer periods
586 (Suliman et al., 2024; Wankmüller et al., 2024), which is reflected in the more stable calibrated
587 thresholds in several clay soil classes and periods (Figure 8). Loamy–silty soils, which have
588 intermediate porosity and water-holding capacity (Ma et al., 2015), exhibit a more mixed
589 behaviour. Although they show clear separation of the SESR signal during pre-sowing, sowing
590 and growing periods (Figure 5c), calibrated SESR thresholds for loamy–silty soils do have skill
591 in the sowing month (Figure 8). These contrasts indicate that SESR-based detection is most
592 reliable where soil moisture deficits persist long enough to affect crops, whereas rapidly draining
593 soils reduce the operational usefulness of SESR as a standalone indicator.



594 The usefulness of calibrated SESR thresholds is governed not only by soil texture but also by
595 the seasonal progression of evaporative stress across crop management periods (Son et al., 2018).
596 During the dry season months that precede the sowing period, high evaporative stress dominates
597 the SESR signal (Noguera et al., 2022; Otkin et al., 2018), producing large variability that often
598 reflects background seasonal drying rather than short-term stress anomalies associated with
599 agricultural impacts (Hobbins and Huntington, 2016). Under these conditions, SESR anomalies
600 may reflect seasonal atmospheric demand rather than crop relevant moisture stress, reducing the
601 reliability of thresholds-based detection. The effect of this background drying on detection
602 performance differs by soil texture. In sandy soils, this short-lived evaporative stress variability
603 produces high false alarm rates (FAR) and weak discrimination in some months (Figure 7),
604 together with the wide uncertainty ranges in calibrated thresholds (Figure 8).

605 Once precipitation begins to moderate evaporative stress (see SESR heatmap across years and
606 months aggregated at each 8-day interval in Figure 2) in the sowing period in May and during
607 the growing period in July for maize and beans (Figure 1), soil moisture is replenished more
608 regularly (Son et al., 2018), which reduces the gap between ET and PET (Hobbins et al., 2019)
609 and also reduces short-term variability in SESR (Noguera et al., 2022). Under these more stable
610 conditions, SESR anomalies can more clearly reflect crop relevant moisture deficits in the soil-
611 period combinations where skilful detection is observed (Anderson et al., 2016). This seasonal
612 transition modifies the SESR signals, but ROC results indicate that skilful discrimination does
613 not increase uniformly after rainfall onset (Figure 7). Instead, skill emerges only in specific soil
614 period combinations, reflecting the interaction between seasonal moisture dynamics and soil
615 water holding capacity. Operationally, this implies that SESR-based flash drought monitoring in
616 dryland agricultural systems should focus on the specific soil-period combinations where skilful
617 detection is observed, rather than applying a uniform approach across all soil textures and
618 months.

619 **4.3 Operational relevance and limitations of calibrated SESR thresholds for flash drought** 620 **monitoring and management** 621

622 The calibrated thresholds reveal context-dependent limitations that must be recognised when
623 integrating SESR into operational drought monitoring. In sandy soils, SESR shows limited
624 ability to distinguish anomalous evaporative stress from background dryness signals (Hobbins
625 and Huntington, 2016; Jabro et al., 2009), resulting in low detection skill and high uncertainty
626 in calibrated thresholds. On the other hand, the skilful thresholds occur predominantly in clay-
627 rich soils, which account for around ~90% of the study area (Figure 1), during pre-sowing,
628 sowing, and growing periods and only during pre-sowing period in loamy–silty textures (Figure
629 8). This spatial and temporal concentration of skilful thresholds indicates that SESR provides
630 operational value only for specific combinations of crop management period and soil texture,
631 and that its performance cannot be assumed outside these domains. Therefore, SESR-based
632 monitoring could not be suitable as a uniformly applied early warning tool across all periods and
633 soils, but rather as a selective component restricted to the conditions where calibrated thresholds
634 demonstrate stability and skill. Even in these settings, SESR-based detections would benefit from
635 verification using complementary information, such as soil moisture indicators, land surface
636 temperature or field-based agronomic observations, to confirm or filter detections (Torelló-
637 Sentelles and Franzke, 2022), and to avoid overinterpreting SESR signals in such settings, as
638 documented in previous studies in dryland regions such as located in Central America (Kibler et



639 al., 2023; Quichimbo et al., 2021; Sun et al., 2019). Additionally, the operational relevance of
640 SESR thresholds depends on the trade-off between high recall and low precision that local
641 governments, managers and farmers are willing to accept (Guimarães Nobre et al., 2023). The
642 choice of the optimal threshold based on the maximum value of F_{β} is conditioned by the
643 parameter β , which determines how the system balances missed events and false alarms (Gallear
644 et al., 2025). In this study, thresholds were selected to favour precision, consistent with a context
645 where false alarms carry high costs (Guimarães Nobre et al., 2019) and institutional response
646 capacity is limited. Under this configuration ($\beta=0.3$), the optimal threshold shifts towards more
647 negative values. This reduces false alarms (FAR) but increases the likelihood of missing early
648 flash drought development. When $\beta=1$, which prioritises recall, thresholds shift toward less
649 negative SESR values, increasing detection under weaker stress and thereby increasing FAR.
650 This behaviour of SESR as an indicator is consistent with findings with other indicators in
651 Halwatura et al., 2017; Gallear et al., 2025; Torelló-Sentelles and Franzke, 2022. As discussed
652 in the literature, decision-makers often avoid acting when uncertainty is high, because the
653 penalties associated with false alarms are visible, whereas the benefits of early actions are less
654 immediately apparent (Bailey, 2012).

655 These decision rules ultimately depend on local decision-makers needing to prioritise
656 (Guimarães Nobre et al., 2019; Lopez and Haines, 2017), and in the rainfed dry corridor of
657 Central America, this statistical trade-off translates directly into an economic one. By mid-May,
658 farmers have already committed financial resources—loans, fertiliser, purchases and labour—
659 (van der Zee Arias et al., 2012). Because flash droughts typically evolve over timescales
660 comparable to the sowing period (~30 days), prioritising precision may reduce false alarms
661 (Gallear et al., 2025) but delay response, thus limiting the opportunity to reschedule planting or
662 implement mitigation (Solh and van Ginkel, 2014). Conversely, favouring recall in May may
663 increase early detection even under weak stress signals (Halwatura et al., 2017) and enable
664 preventive action, but at potentially high implementation costs. In line with principles discussed
665 in the impact-based forecasting (Shyrokaya et al., 2024), a more appropriate strategy would be
666 to redefine the objective function according to economic risk (Bailey, 2012; Portele et al., 2021;
667 Salmoral et al., 2019) and cost-loss analysis (Zhu et al., 2002), as well as the participation of
668 stakeholders rather than purely statistical criteria (McEwen et al., 2021). Although this study
669 dynamically adjusted the optimal thresholds to reflect the spatial and temporal variability,
670 considering crop management periods and soil textures, fully operational deployment would
671 require extending this approach to explicitly account for economic risk and decision-making
672 constraints.

673 5. Conclusions

674

675 In this study, a context-specific threshold calibration approach was developed to improve the
676 spatial and temporal detection of agricultural flash drought conditions in support of drought
677 monitoring and management. The study was conducted in the Central America Dry Corridor, a
678 dryland region in Nicaragua that is representative of rainfed agricultural systems exposed to
679 short-lived but intense evaporative stress found in many tropical drylands worldwide. The
680 approach uses the Standardized Evaporative Stress Ratio (SESR), together with its rate of change
681 (Δ SESR), and calibrates SESR thresholds using two benchmarks of observed drought-induced
682 crop loss impacts. Calibrated SESR thresholds were evaluated across crop management periods
683 and soil textures. The conclusions are summarised below:

684



- 685
- 686
- 687
- 688
- 689
- 690
- 691
- 692
- 693
- 694
- 695
- 696
- 697
- 698
- 699
- 700
- 701
- 702
- 703
- 704
- 705
- 706
- 707
- 708
- 709
- 710
- 711
- 712
- 713
- 714
- 715
- 716
- 717
- 718
- 719
- 720
- 721
- 722
- Although SESR contains coherent signals of evaporative stress intensification during years with drought-induced crop losses, default thresholds used in the literature do not translate this signal into a useful indicator of agricultural relevance. These default thresholds frequently identify stress conditions in years without reported losses while failing to capture the more extreme SESR values at which agricultural impacts are observed in this dryland context. As a result, literature-based thresholds show limited suitability for operational flash drought monitoring in the study region.
 - Calibrated thresholds reveal that the detectability of agriculturally relevant flash drought conditions using SESR depends jointly on crop management periods and soil textures. Skilful thresholds could not be found in sandy soils, where rapid soil moisture fluctuations limit the persistence of evaporative stress signals rather than the occurrence of agricultural impacts themselves. In contrast, clay-rich soils exhibit stable and skilful thresholds during specific crop management periods within pre-sowing, sowing and growing periods (April to July), with the skilful months varying among individual clay-rich soils classes. Loamy–silty soils showed intermediate behaviour, with skilful thresholds only in March and the pre-sowing period in April. These results indicate that SESR-based flash drought detection cannot be generalised uniformly across space or time but instead depends on the interaction between soil hydraulic properties and seasonal evolution of evaporative stress.
 - Validation against the agricultural benchmarks confirms that calibrated thresholds detect flash drought conditions more frequently in years that also exhibit drought-induced crop losses than literature-based thresholds, while still producing detections in some years without reported losses and missing impacts in others. This indicates that SESR thresholds can provide operationally relevant but conditional information, with useful performance confined to specific soil-crop management period combinations, particularly during the growing period, where threshold stability and detection skill are jointly satisfied. More broadly, these findings support ongoing effort toward impact-based drought monitoring and early warning by showing that physically based indicators such as SESR require calibration against observed agricultural impacts to be operationally meaningful. Rather than assuming that evaporative stress thresholds alone are sufficient to indicate agricultural impacts, this study demonstrates that linking SESR-based stress signals to crop losses and crop management periods improves their relevance for agricultural decision-making. At the same time, the results highlight that fixed percentile thresholds are insufficient in heterogeneous dryland environments, where translation from physical stress to agricultural impact is strongly context dependent.

723 This research provides temporally and spatially calibrated thresholds for agricultural flash
724 drought detection in the Central America Dry Corridor, further work is needed to generalise and
725 deepen these findings. As the approach itself is generalisable, future research should test the skill
726 of flash drought detection using calibrated thresholds in other dryland regions and cropping
727 systems. Additionally, further research should explore adding complementary variables in
728 settings where SESR alone does not sufficiently discriminate impact-relevant stress conditions.
729 Finally, threshold selection cannot be reduced to mechanical optimisation of statistical metrics;
730 effective operational use requires explicit consideration of economic risk, stakeholder priorities,
731 and the asymmetric consequences of missed events and false alarms so that SESR-based alerts
732 support timely, informed, and context-appropriate decision-making for farmers and institutions.



733 **6. Data availability and code**

734 The data and code are available on request.

735 **7. Author contributions**

736 IU-T: conceptualisation (lead), methodology (lead), investigation (lead), formal analysis (lead),
737 data curation and coding (lead), visualisation (lead), writing original draft, review and editing
738 (lead), funding acquisition (lead). MW: conceptualisation (lead), methodology (lead), and
739 supervision (lead). CB and MC, conceptualisation (supporting), methodology (supporting),
740 supervision (supporting), GJ: conceptualisation (supporting), methodology (supporting),
741 supervision (supporting), funding acquisition (lead). The first draft was written by IU-T, and all
742 authors commented on previous versions of the manuscript.

743 **8. Competing of interests**

744 The author declares that none of the authors has any competing interests.

745 **9. Acknowledgments**

746 The author thanks the Schlumberger Foundation Faculty for the Future Fellowship Program for
747 their financial support.

748 **10. Financial support**

749 This work was financially supported by the Schlumberger Foundation Faculty for the Future
750 Fellowship Program.

751 **11. Bibliography**

752 Anderson, M. C., Zolin, C. A., Sentelhas, P. C., Hain, C. R., Semmens, K., Tugrul Yilmaz, M.,
753 Gao, F., Otkin, J. A., Tetrault, R. The evaporative stress index as an indicator of agricultural
754 drought in Brazil: an assessment based on crop yield impacts, *Remote Sens. Environ.*, 174, 82–
755 99, <https://doi.org/10.1016/j.rse.2015.11.034>, 2016.

756 Bailey, R. *Famine early warning and early action: the cost of delay*. Chatham House, London,
757 24 pp., 2012.
758 https://www.chathamhouse.org/sites/default/files/public/Research/Energy,%20Environment%20and%20Development/0712pr_bailey.pdf

760 Basara, J. B., Christian, J. I., Wakefield, R. A., Otkin, J. A., Hunt, E. H., Brown, D. P. The
761 evolution, propagation, and spread of flash drought in the Central United States during 2012,
762 *Environ. Res. Lett.*, 14, 084025, <https://doi.org/10.1088/1748-9326/ab2cc0>, 2019.

763 Bucheli, J., Dalhaus, T., Finger, R. The optimal drought index for designing weather index
764 insurance, *Eur. Rev. Agric. Econ.*, 48, 573–597, <https://doi.org/10.1093/erae/jbaa014>, 2021.

765 Buitink, J., van Hateren, T. C., Teuling, A. J. Hydrological system complexity induces a
766 drought frequency paradox, *Front. Water*, 3, 640976,
767 <https://doi.org/10.3389/frwa.2021.640976>, 2021.

768 Cao, K., Wei, C., Gaidon, A., Arechiga, N., Ma, T. Learning imbalanced datasets with label-
769 distribution-aware margin loss, *Adv. Neural Inf. Process. Syst.*, 32, 1567–1578, 2019.

770 Christian, J. I., Basara, J. B., Otkin, J. A., Hunt, E. D., Wakefield, R. A., Flanagan, P. X., Xiao,
771 X. A methodology for flash drought identification: application of flash drought frequency



- 772 across the United States, *J. Hydrometeorol.*, 20, 833–846, [https://doi.org/10.1175/JHM-D-18-](https://doi.org/10.1175/JHM-D-18-0198.1)
773 0198.1, 2019.
- 774 DGOT–INETER. Atlas nacional de suelos de la República de Nicaragua. Managua, Nicaragua,
775 2024. <https://www.ineter.gob.ni/mapa/pub/atlassuelo/1erAtlasNacionaldeSuelos.pdf>
- 776 Edris, S. G., Basara, J. B., Christian, J. I., Hunt, E. D., Otkin, J. A., Salesky, S. T., Illston, B. G.
777 Analysis of the critical components of flash drought using the standardized evaporative stress
778 ratio, *Agric. For. Meteorol.*, 330, 109288, <https://doi.org/10.1016/j.agrformet.2022.109288>,
779 2023.
- 780 Efron, B., Tibshirani, R. Bootstrap methods for standard errors, confidence intervals, and other
781 measures of statistical accuracy, *Stat. Sci.*, 1, 54–75, <https://doi.org/10.1214/ss/1177013815>,
782 1986.
- 783 FAO. Vegetation health index near real time (Global - dekadal - 1 km) - ASIS (raster), FAO,
784 2014. <https://www.fao.org/giews/earthobservation/access.jsp>
- 785 Fuganti, G., Minelli, M., Rojas, O. Practical guidelines for early warning–early action plans on
786 agricultural drought. FAO, Rome, Italy, 2020. [https://openknowledge.fao.org/items/dd8ad74b-](https://openknowledge.fao.org/items/dd8ad74b-8c2f-40e6-b899-62e52d2aad07)
787 8c2f-40e6-b899-62e52d2aad07
- 788 Gallear, J. W., Valadares Galdos, M., Zeri, M., Hartley, A. Evaluation of machine learning
789 approaches for large-scale agricultural drought forecasts to improve monitoring and
790 preparedness in Brazil, *Nat. Hazards Earth Syst. Sci.*, 25, 1521–1541,
791 <https://doi.org/10.5194/nhess-25-1521-2025>, 2025.
- 792 Ghasemi, A., Zahediasl, S. Normality tests for statistical analysis: a guide for non-statisticians,
793 *Int. J. Endocrinol. Metab.*, 10, 486–489, <https://doi.org/10.5812/ijem.3505>, 2012.
- 794 Gou, Q., Zhu, Y., Lü, H., Horton, R., Yu, X., Zhang, H., Wang, X., Su, J., Liu, E., Ding, Z.,
795 Wang, Z., Yuan, F. Application of an improved spatio-temporal identification method of flash
796 droughts, *J. Hydrol.*, 604, 127224, <https://doi.org/10.1016/j.jhydrol.2021.127224>, 2022.
- 797 Gu, Y., Wylie, B. K., Howard, D. M., Phuyal, K. P., Ji, L. NDVI saturation adjustment: a new
798 approach for improving cropland performance estimates in the Greater Platte River Basin,
799 USA, *Ecol. Indic.*, 30, 1–6, <https://doi.org/10.1016/j.ecolind.2013.01.041>, 2013.
- 800 Guimarães Nobre, G., Davenport, F., Bischiniotis, K., Veldkamp, T., Jongman, B., Funk, C.
801 C., Husak, G., Ward, P. J., Aerts, J. C. J. H. Financing agricultural drought risk through ex-ante
802 cash transfers, *Sci. Total Environ.*, 653, 523–535, 653, 523–535,
803 <https://doi.org/10.1016/j.scitotenv.2018.10.406>, 2019.
- 804 Guimarães Nobre, G., Pasqui, M., Quaresima, S., Pieretto, S., Lemos Pereira Bonifácio, R. M.
805 Forecasting, thresholds, and triggers: towards developing a forecast-based financing system for
806 droughts in Mozambique, *Clim. Serv.*, 30, 100344,
807 <https://doi.org/10.1016/j.cliser.2023.100344>, 2023.
- 808 Halwatura, D., McIntyre, N., Lechner, A. M., Arnold, S. Capability of meteorological drought
809 indices for detecting soil moisture droughts, *J. Hydrol.: Reg. Stud.*, 12, 396–412,
810 <https://doi.org/10.1016/j.ejrh.2017.06.001>, 2017.



- 811 Hobbins, M. T., Huntington, J. L. Evapotranspiration and evaporative demand. In: Singh, V. P.
812 (Ed.), *Handbook of applied hydrology*, 2nd ed., McGraw-Hill Education, New York, USA,
813 42.1–42.18, 2016.
- 814 Hobbins, M., Dewes, C., Huntington, J. L. Evaporative demand: dynamics and opportunities in
815 drought early warning, monitoring, and vulnerability assessment. In: *Proceedings of the Sixth*
816 *Interagency Conference on Research in the Watersheds*, DRI, Shepherdstown, USA, 211,
817 2019.
- 818 INETER, ANA, UNI, and GIZ-PROATAS: Cuencas Hidrográficas de Nicaragua bajo la
819 metodología Pfafstetter, 2014. [https://cira.unan.edu.ni/wp-content/uploads/2016/07/Album-](https://cira.unan.edu.ni/wp-content/uploads/2016/07/Album-Cuencas-Nic-Revisado_ANA.pdf)
820 [Cuencas-Nic-Revisado_ANA.pdf](https://cira.unan.edu.ni/wp-content/uploads/2016/07/Album-Cuencas-Nic-Revisado_ANA.pdf)
- 821 Jabro, J. D., Evans, R. G., Kim, Y., Iversen, W. M. Estimating in situ soil–water retention and
822 field water capacity in two contrasting soil textures, *Irrig. Sci.*, 27, 223–229,
823 <https://doi.org/10.1007/s00271-008-0137-9>, 2009.
- 824 Kibler, C. L., Trugman, A. T., Roberts, D. A., Still, C. J., Scott, R. L., Caylor, K. K., Stella, J.
825 C., Singer, M. B. Evapotranspiration regulates leaf temperature and respiration in dryland
826 vegetation, *Agric. For. Meteorol.*, 339, 109560,
827 <https://doi.org/10.1016/j.agrformet.2023.109560>, 2023.
- 828 Kogan, F. N. Application of vegetation index and brightness temperature for drought detection,
829 *Adv. Space Res.*, 15, 91–100, [https://doi.org/10.1016/0273-1177\(95\)00079-T](https://doi.org/10.1016/0273-1177(95)00079-T), 1995.
- 830 Kozlowski, T. T.: *Water deficits and plant growth*, Academic Press, New York, 1968.
- 831 Leasor, Z. T., Quiring, S. M., Svoboda, M. D. Utilizing objective drought severity thresholds to
832 improve drought monitoring, *J. Appl. Meteorol. Climatol.*, 59, 1455–1470,
833 <https://doi.org/10.1175/JAMC-D-19-0217.1>, 2020.
- 834 Li, X., Piao, S., Huntingford, C., Peñuelas, J., Yang, H., Xu, H., Chen, A., Friedlingstein, P.,
835 Keenan, T. F., Sitch, S., Wang, X., Zscheischler, J., Mahecha, M. D. Global variations in
836 critical drought thresholds that impact vegetation, *Natl. Sci. Rev.*, 10, nwad049,
837 <https://doi.org/10.1093/nsr/nwad049>, 2023.
- 838 Lopez, A., Haines, S. Exploring the usability of probabilistic weather forecasts for water
839 resources decision-making in the United Kingdom, *Weather Clim. Soc.*, 9, 701–715,
840 <https://doi.org/10.1175/WCAS-D-16-0072.1>, 2017.
- 841 Lovino, M. A., Pierrestegui, M. J., Müller, O. V., Müller, G. V., Berbery, E. H. The prevalent
842 life cycle of agricultural flash droughts, *npj Clim. Atmos. Sci.*, 7, 1–11,
843 <https://doi.org/10.1038/s41612-024-00618-0>, 2024.
- 844 Ma, W., Zhang, X., Zhen, Q., Zhang, Y. Effect of soil texture on water infiltration in semiarid
845 reclaimed land, *Water Qual. Res. J.*, 51, 33–41, <https://doi.org/10.2166/wqrjc.2015.025>, 2015.
- 846 Marzban, C. The ROC curve and the area under it as performance measures, *Weather*
847 *Forecast.*, 19, 1106–1114, <https://doi.org/10.1175/825.1>, 2004.
- 848 McEwen, L., Bryan, K., Black, A., Blake, J., Afzal, M. Science-narrative explorations of
849 drought thresholds in the maritime Eden catchment, Scotland: implications for local drought



- 850 risk management, *Front. Environ. Sci.*, 9, 589980, <https://doi.org/10.3389/fenvs.2021.589980>,
851 2021.
- 852 Nan, Y., Chai, K. M., Lee, W. S., Chieu, H. L. Optimizing F-measure: a tale of two
853 approaches, *Proc. 29th Int. Conf. Mach. Learn.*, arXiv:1206.4625,
854 <https://doi.org/10.48550/arXiv.1206.4625>, 2012.
- 855 Nguyen, N. M., Choi, M. Delving into flash droughts in Vietnam during last two decades using
856 the standardized evaporative stress ratio, *J. Hydrol.*, 634, 130669,
857 <https://doi.org/10.1016/j.jhydrol.2024.130669>, 2024.
- 858 Noguera, I., Vicente-Serrano, S. M., Domínguez-Castro, F. The rise of atmospheric
859 evaporative demand is increasing flash droughts in Spain during the warm season, *Geophys.*
860 *Res. Lett.*, 49, e2021GL097703, <https://doi.org/10.1029/2021GL097703>, 2022.
- 861 Or, D., Lehmann, P. Surface evaporative capacitance: how soil type and rainfall characteristics
862 affect global-scale surface evaporation, *Water Resour. Res.*, 55, 519–539,
863 <https://doi.org/10.1029/2018WR024050>, 2019.
- 864 Otkin, J. A., Svoboda, M., Hunt, E. D., Ford, T. W., Anderson, M. C., Hain, C., and Basara, J.
865 B.: Flash Droughts: A Review and Assessment of the Challenges Imposed by Rapid-Onset
866 Droughts in the United States, *Bulletin of the American Meteorological Society*, 99, 911–919,
867 <https://doi.org/10.1175/BAMS-D-17-0149.1>, 2018.
- 868 Otkin, J. A., Svoboda, M., Hunt, E. D., Ford, T. W., Anderson, M. C., Hain, C., Basara, J. B.
869 Flash droughts: a review and assessment of the challenges imposed by rapid-onset droughts in
870 the United States, *Bull. Am. Meteorol. Soc.*, 99, 911–919, <https://doi.org/10.1175/BAMS-D-21-0288.1>, 2022.
- 872 Padiyedath Gopalan, S., Kawamura, A., Amaguchi, H., Takasaki, T., Azhikodan, G. A
873 bootstrap approach for the parameter uncertainty of an urban-specific rainfall–runoff model, *J.*
874 *Hydrol.*, 579, 124195, <https://doi.org/10.1016/j.jhydrol.2019.124195>, 2019.
- 875 Portele, T. C., Lorenz, C., Dibrani, B., Laux, P., Bliefernicht, J., Kunstmann, H. Seasonal
876 forecasts offer economic benefit for hydrological decision making in semi-arid regions, *Sci.*
877 *Rep.*, 11, 10581, <https://doi.org/10.1038/s41598-021-89564-y>, 2021.
- 878 Quichimbo, E. A., Singer, M. B., Michaelides, K., Hobley, D. E. J., Rosolem, R., Cuthbert, M.
879 O. DRYP 1.0: a parsimonious hydrological model of dryland partitioning of the water balance,
880 *Geosci. Model Dev.*, 14, 6893–6917, <https://doi.org/10.5194/gmd-14-6893-2021>, 2021.
- 881 Rojas, O. Agricultural extreme drought assessment at global level using the FAO-Agricultural
882 Stress Index System (ASIS), *Weather Clim. Extremes*, 27, 100184,
883 <https://doi.org/10.1016/j.wace.2018.09.001>, 2020.
- 884 Rojas, O., Rodríguez de España, M. V., Hernández, T. New canicula index to study its impact
885 on agriculture in the Central American Dry Corridor and its connection with El Niño, FAO,
886 Rome, Italy, 67 pp., <https://doi.org/10.4060/cb1818es>, 2020.
- 887 Salinas Marcenaro, I., Jarquin Diaz, J. R., Ortega Flores, G. J., Téllez Reyes, A. L. La
888 evapotranspiración potencial en Nicaragua usando sensores remotos. Universidad Nacional
889 Agraria, Managua, Nicaragua, 2023. <https://repositorio.una.edu.ni/4715/1/REN40U58.pdf>,



- 890 Salmoral, G., Rey, D., Rudd, A., de Margon, P., Holman, I. A probabilistic risk assessment of
891 the national economic impacts of regulatory drought management on irrigated agriculture,
892 *Earths Future*, 7, 178–196, <https://doi.org/10.1029/2018EF001092>, 2019.
- 893 Sawilowsky, S. Misconceptions leading to choosing the t test over the Wilcoxon Mann-
894 Whitney test for shift in location parameter, *J. Mod. Appl. Stat. Methods*, 4, 598–600,
895 <https://doi.org/10.22237/jmasm/1130804700>, 2005.
- 896 Shyrokaya, A., Pappenberger, F., Pechlivanidis, I., Messori, G., Khatami, S., Mazzoleni, M.,
897 Di Baldassarre, G. Advances and gaps in the science and practice of impact-based forecasting
898 of droughts, *WIREs Water*, 11, e1698, <https://doi.org/10.1002/wat2.1698>, 2024.
- 899 Solh, M., van Ginkel, M. Drought preparedness and drought mitigation in the developing
900 world’s drylands, *Weather Clim. Extremes*, 3, 62–66,
901 <https://doi.org/10.1016/j.wace.2014.03.003>, 2014.
- 902 Soltani, A., Meinke, H., de Voil, P. Assessing linear interpolation to generate daily radiation
903 and temperature data for use in crop simulations, *Eur. J. Agron.*, 21, 133–148,
904 [https://doi.org/10.1016/S1161-0301\(03\)00044-3](https://doi.org/10.1016/S1161-0301(03)00044-3), 2004.
- 905 Son, N.-T., Chen, C.-F., Chen, C.-R., Castellón, A., Masferrer, M.-G.-M., Recinos, L.-E.-M.
906 Satellite characterization of drought over cultivated areas in Central America, *Int. J. Remote
907 Sens.*, 39, 8505–8526, <https://doi.org/10.1080/01431161.2018.1488287>, 2018.
- 908 Steve, R., Qiaozhen, M., Maosheng, Z., and Alvaro, M. MODIS/Aqua Net Evapotranspiration
909 Gap-Filled Yearly L4 Global 500m SIN Grid V061,
910 <https://doi.org/10.5067/MODIS/MYD16A3GF.061>, 2021.
- 911 Suliman, M., Scaini, A., Manzoni, S., Vico, G. Soil properties modulate actual
912 evapotranspiration, and precipitation impacts on crop yields in the USA, *Sci. Total Environ.*,
913 949, 175172, <https://doi.org/10.1016/j.scitotenv.2024.175172>, 2024.
- 914 Sun, X., Wilcox, B. P., Zou, C. B. Evapotranspiration partitioning in dryland ecosystems: a
915 global meta-analysis of in situ studies, *J. Hydrol.*, 576, 123–136,
916 <https://doi.org/10.1016/j.jhydrol.2019.06.022>, 2019.
- 917 Svoboda, M., LeComte, D., Hayes, M., Heim, R., Gleason, K., Angel, J. J. R. J., Rippey, B.,
918 Tinker, R., Palecki, M., Stooksbury, D., Miskus, D., Stephens, D. The Drought Monitor, *Bull.
919 Am. Meteorol. Soc.*, 83, 1181–1190, [https://doi.org/10.1175/1520-0477\(2002\)083%253C1181:TDM%253E2.3.CO;2](https://doi.org/10.1175/1520-0477(2002)083%253C1181:TDM%253E2.3.CO;2), 2002.
- 921 Teleubay, Z., Quiring, S. M., Leasor, Z. Estimation of impacts-based drought thresholds for the
922 U.S. Corn Belt, *Agric. For. Meteorol.*, 372, 110715,
923 <https://doi.org/10.1016/j.agrformet.2025.110715>, 2025.
- 924 Teluguntla, P., Thenkabail, P., Oliphant, A., Gumma, M., Aneece, I., Foley, D., McCormick,
925 R. Landsat-derived global rainfed and irrigated-cropland product, 30 m, version 001, NASA
926 EOSDIS Land Processes DAAC,
927 <https://doi.org/10.5067/COMMUNITY/LGRIP/LGRIP30.001>, 2023.
- 928 Teoh, K. K., Ibrahim, H., Bejo, S. K. Investigation on several basic interpolation methods for
929 use in remote sensing application, in 2008 IEEE Conference on Innovative Technologies in



- 930 Intelligent Systems and Industrial Applications, 60–65,
931 <https://doi.org/10.1109/CITISIA.2008.4607336>, 2008.
- 932 Torelló-Sentelles, H., Franzke, C. L. E. Drought impact links to meteorological drought
933 indicators and predictability in Spain, *Hydrol. Earth Syst. Sci.*, 26, 1821–1844,
934 <https://doi.org/10.5194/hess-26-1821-2022>, 2022.
- 935 Tu, Z., Yang, Y. On the estimation of potential evaporation under wet and dry conditions,
936 *Water Resour. Res.*, 58, e2021WR031486, <https://doi.org/10.1029/2021WR031486>, 2022.
- 937 Ubeda Trujillo, I., Rocha, L. Dinámica de coberturas de la tierra en la subcuenca III de la
938 cuenca sur del Lago de Managua, Nicaragua, *Rev. Torreón Univ.*, 9, 110–128,
939 <https://doi.org/10.5377/torreon.v9i25.9857>, 2020.
- 940 Verbist, K., Maureira, H., Aroche, R. Midsummer drought atlas for Central America and the
941 Caribbean. Water Centre for Arid and Semi-arid Zones of Latin America and the Caribbean
942 (UNESCO), 46 pp., 2018.
- 943 Wankmüller, F. J. P., Delval, L., Lehmann, P., Baur, M. J., Cecere, A., Wolf, S., Or, D.,
944 Javaux, M., Carminati, A. Global influence of soil texture on ecosystem water limitation,
945 *Nature*, 635, 631–636, <https://doi.org/10.1038/s41586-024-08089-2>, 2024.
- 946 Yu, M., Zhang, J., Wei, L., Wang, G., Dong, W., Liu, X. Impact of soil textures on agricultural
947 drought evolution and field capacity estimation in humid regions, *J. Hydrol.*, 626, 130257,
948 <https://doi.org/10.1016/j.jhydrol.2023.130257>, 2023.
- 949 Yuan, X., Wang, L., Wu, P., Ji, P., Sheffield, J., Zhang, M. Anthropogenic shift towards higher
950 risk of flash drought over China, *Nat. Commun.*, 10, 4661, <https://doi.org/10.1038/s41467-019-12692-7>, 2019.
- 952 Yuan, X., Wang, Y., Ji, P., Wu, P., Sheffield, J., Otkin, J. A. A global transition to flash
953 droughts under climate change, *Science.*, 380, 187–191,
954 <https://doi.org/10.1126/science.abn6301>, 2023.
- 955 van der Zee Arias, A., van der Zee, J., Meyrat, A., Poveda, C., Picado, L. Estudio de
956 caracterización del Corredor Seco Centroamericano. FAO, Tegucigalpa, Honduras, 2012.
957 <https://bibliotecasemiarios.ufv.br/jspui/handle/123456789/367>
- 958 Zhu, Y., Toth, Z., Wobus, R., Richardson, D., Mylne, K. Economic value of ensemble-based
959 weather forecasts, *Bull. Am. Meteorol. Soc.*, 83, 73–83, [https://doi.org/10.1175/1520-0477\(2002\)083<0073:TEVOEB>2.3.CO;2](https://doi.org/10.1175/1520-0477(2002)083<0073:TEVOEB>2.3.CO;2), 2002.